Robotica (2023), **41**, pp. 3137–3159
doi:10.1017/S0263574723000929

CAMBRIDGE UNIVERSITY PRESS

RESEARCH ARTICLE

Kinematic and dynamic analysis of a 4-DOF over-constraint parallel driving mechanism with planar sub-closed chains

Yangyang Huang[1], Jinzhu Zhang[1,2], Xiaoyan Xiong[1,2] and Shengxiang Liu[1]

[1]College of Mechanical and Vehicle Engineering, Taiyuan University of Technology, Taiyuan, China and [2]Engineering Research Center of Advanced Metal Composites Forming Technology and Equipment, Ministry of Education, Taiyuan, China
Corresponding author: Jinzhu Zhang; E-mail: zhangjinzhu@tyut.edu.cn

Received: 13 March 2023; **Revised:** 9 May 2023; **Accepted:** 13 June 2023; **First published online:** 19 July 2023

Keywords: low-mobility parallel driving mechanism; over-constrained; sub-closed chains; kinematics; force analysis

Abstract

In this paper, a new over-constrained parallel driving mechanism (PDM) with planar sub-closed chains is proposed. First, the number of over-constraints on the PDM is calculated. Then, an analysis is conducted as to the kinematics of the hybrid manipulator, including positions, velocities, and accelerations of all bodies. Furthermore, the Newton–Euler approach is taken to deduce the kinematic formula of each link and the formula of inertial force at the center of mass. However, it remains difficult to solve the equation since the number of equations is smaller than that of unknown variables. To solve this problem, the screw theory is applied in the present study to analyze the cause of over-constraints, with the link's elastic deformation introduced as the supplement of deformation compatibility equations. Moreover, the actuation forces and constrained forces/moments are calculated simultaneously. Finally, the dynamic model is verified through simulation and experimentation. The proposed modeling approach provides a fundamental basis for the structural optimization and friction force computation of the over-constrained PDM.

1. Introduction

The creative design of mechanisms is widely regarded as one of the most important branches of the theory of mechanisms [1]. As a new type of mechanism, parallel driving mechanism (PDM) [2] represents a subset of hybrid manipulator [3–5]. By definition, the PDM consists of an operating mechanism, multiple driving mechanisms, and connecting joints. Based on this, this paper proposed a 2T2R PDM. The 2T2R manipulator organically combines spatial translation and rotation, and is widely used in industry. For example, this manipulator can be combined with linear guide rail to form a five-axis linkage CNC machine tool [6, 7] and can also be used as motion simulator [8], vibration isolation platform [9], and so on. Among which, CNC machine tools have requirements for high accuracy of the manipulator, while the others have certain requirements for high-frequency and high-acceleration characteristics. In general, the PDM involves more sub-closed loops [10, 11] and over-constraints [12, 13]. Excluding actuators, its operating mechanism is independent of the driving mechanism, which makes the mechanism perform well in terms of structural stiffness [14, 15] and high acceleration [16, 17]. Similar to parallel mechanisms, the PDM has drawbacks such as small workspace, difficulty in solving forward kinematics, and complex control. In addition, there are new challenges in dynamic modeling due to over-constraints and the closed-loop structure.

In contrast to the open-chain serial manipulators, the dynamic analysis of parallel manipulators is inherently complex due to their closed-loop structure. Nevertheless, dynamic modeling plays an

essential role in structural design and control scheme design for parallel manipulators. However, the requirements for dynamic models are different, which depends on the exact application. For the control scheme design, the dynamic model must be efficient enough for the real-time calculation; for the structural design, it is necessary to calculate the driving forces/torque and the constrained forces/moments simultaneously [18]. In general, dynamic modeling methods [19–21] can be divided into four categories: Lagrangian formula [22, 23], Newton–Euler method [18, 24, 25], virtual work principle [26, 27], and Kane equation [28]. Among them, the Lagrangian formula is advantageous in solving the driving force of manipulator, with its explicit dynamic form conducive to dynamic analysis and control. Newton–Euler method can be used not only to solve the driving force but also to solve all the constraints/torques of joints effectively. However, the number of equations is generally smaller than the unknown number under the over-constrained mechanism, which makes it challenging to solve the dynamic model. At present, there have been some studies conducted on the dynamic modeling of the over-constrained parallel manipulators. Xu et al. [29] proposed a new approach to the force analysis of over-constrained parallel mechanisms with lower mobility parallel mechanism, with consideration given to the spatial compound elastic deformation of the rod. Chen et al. [18] used the Newton–Euler formula and the natural orthogonal complement method to establish dynamic models with and without constraint force/moment simultaneously, with the deformation caused by over-constraint force/moment deduced. Bi et al. [30] constructed the dynamic model of the over-constrained mechanism Exechon by combining Newton–Euler formula with compliance conditions. The established dynamic model can be combined with the control system to improve the precision and dynamic performance of real-time control. For a mechanism subjected to the active and passive redundant constraints without parasitic motion, Chen et al. [31] established an efficient dynamic model in line with the principle of virtual work by introducing classical optimization criteria and deformation coordination conditions. To sum up, the above-mentioned studies have contributed great ideas to solving the over-constrained mechanisms.

As can be seen from the above, introducing link flexibility is a common method for analyzing over-constrained mechanisms. The links' elastic deformation can not only supplement the deformation coordination equation [32, 33] in the over-constrained direction but also cause pose error of the end-effector. The former provides a basis for the lightweight design. It focuses on using the links' elastic deformation to solve the constraint force/moment [34] and joint friction [35] of the manipulator. As for the latter, it focuses on the impact of the rigid–flexible coupling [36–38] characteristics, large-range rigid body motion, and the elastic deformation of the rod, on the errors in position and orientation of the end-effector. However, the hybrid manipulator is free from large-range rigid body motion in the over-constrained direction, and the link flexibility conforms to the assumption of linear elasticity and small deformation. Therefore, it is proposed in this paper to supplement the deformation compatibility equation in the over-constrained direction by introducing the flexibility matrix and the superposition principle into the process of theoretical calculation. To facilitate simulation, the assumed mode method is used for the link flexibility in ABAQUS. Then, dynamic verification is carried out using the rigid–flexible coupling dynamic model of the co-simulation of ADAMS and ABAQUS.

To sum up, there have been some methods developed to solve the over-constraint issue. However, the PDM is still more challenging than the traditional parallel mechanism in terms of structural complexity and static indeterminate times. In addition, sub-closed loops are another characteristic of PDM, and the over-constrained mechanisms containing sub-closed loops [39, 40] are usually coupled in a nonlinear manner, which makes it difficult to conduct kinematic and dynamic analysis of them [19, 41, 42]. At present, there are still few reports on the dynamic modeling of the PDMs. In this paper, with a new 4-DOF PDM as the research object, the over-constrained direction is first analyzed through the screw theory. Then, the flexibility matrix and superposition principle are introduced to supplement the deformation compatibility equation in the over-constrained direction. Finally, a complete dynamic model involving all active forces/moments and restraint forces/moments is constructed. This modeling method is also applicable to other over-constrained PDMs.

https://doi.org/10.1017/S0263574723000929 Published online by Cambridge University Press

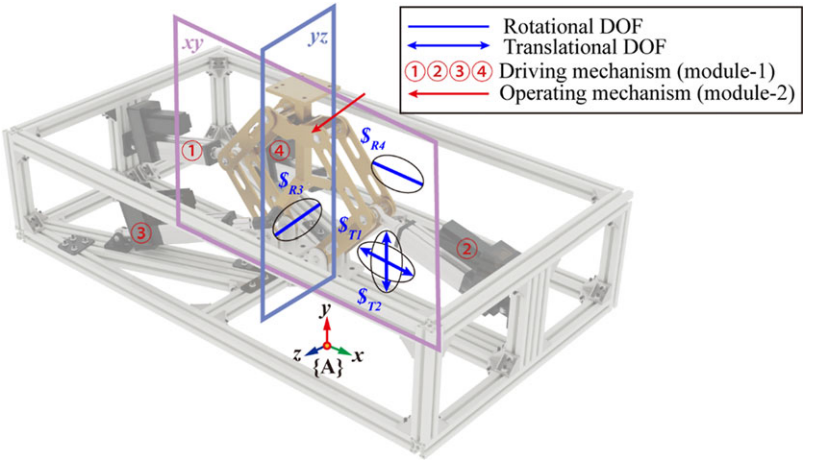

Figure 1. *Virtual prototype for the 4-DOF PDM.*

The remainder of this paper is organized as follows. In Section 2, the system conceptual design is described. Then, the kinematics modeling of the PDM is detailed in Section 3, where the positions, velocities, and accelerations of all bodies in the manipulator are determined. In Section 4, dynamics modeling is performed using the Newton–Euler method. Moreover, compatibility equations are introduced in Section 5 to solve the over-constraint forces/moments. Then, numerical simulations and experiments are conducted in Section 6. Lastly, the conclusions of this study are drawn in Section 7.

2. System conceptual design

2.1. Mechanism configuration design

In this paper, a new 4-DOF PDM with two rotational DOFs and two translational DOFs is taken as the research object. The virtual prototype for the mechanism is represented in Fig. 1. $\$_{T1}$ and $\$_{T2}$ denote the translation along x-axis and y-axis, respectively. $\$_{R3}$ and $\$_{R4}$ represent rotation around z-axis and x-axis, respectively. The 4-DOF PDM is composed of a fixed platform, a moving platform (MP), an operating mechanism and driving mechanisms. The driving mechanisms consist of four distributed limbs, with two identical RPR limbs and two identical SPU limbs. Each limb is formed by a cylinder and a piston and the prismatic joints of limbs are actuated, which are the inputs of the system, the position and orientation of the MP is the output. The operating mechanism consists of a six-bar mechanism and a revolute joint in series. As shown in Fig. 2, R_{1i}, R_{2i}, R_{3i}, R_{4i}, and $R_4 (i = 1, 2)$ represent the revolute joint; $U_{2j} (j = 3, 4)$ represents the universal joint; S_{2j} denotes the spherical joint; P_{1i} and P_{2j} represent the prismatic joint. The reference frame $\boldsymbol{P}$-xyz and the moving frame $\boldsymbol{A}$-xyz are attached to the MP and the base, respectively. l_{1i} and l_{2j} denote the location of the prismatic joint in each limb. The geometric parameters are given in Appendix A.

2.2. Workspace analysis

The boundary of the reachable workspace is determined with the help of boundary search method as shown in Fig. 3(a), where the z-axis is parasitic motion. Figure 3(b) shows its projection in the x–y direction. The link extensions, l_{11}, l_{12}, l_{23}, and l_{24}, are limited between -50 (mm) and 50 (mm) since the left and right grounded prismatic links are assumed to be physically constrained by the ground at those boundary angles. In addition, other link angles are also subject to certain constraints based on physical properties.

https://doi.org/10.1017/S0263574723000929 Published online by Cambridge University Press

Table I. *Joint type and number of the 4-DOF PDM.*

Joint	Symbol	Value
Active component	n	14
Spherical joint	S	2
Universal joint	U	2
Revolute joint	R	11
Prismatic joint	P	4
Actuator	A	4

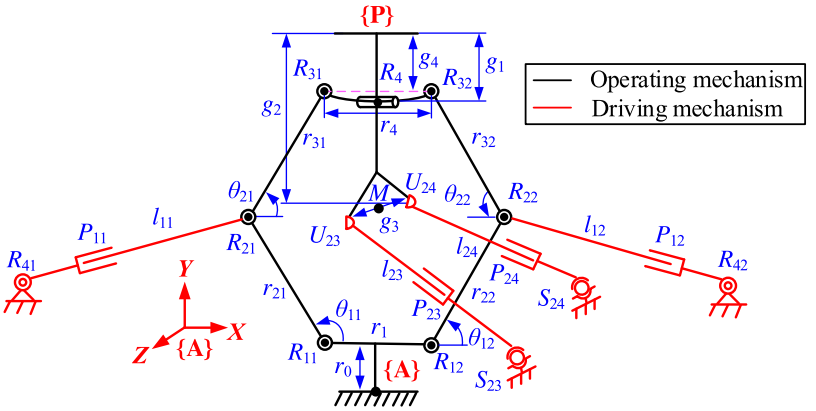

Figure 2. *Schematic diagram of the 4-DOF PDM.*

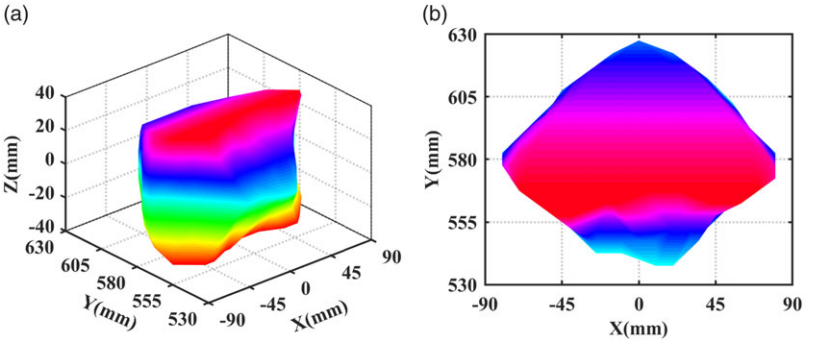

Figure 3. *The reachable workspace of the 4-DOF PDM.*

2.3. Over-constraint analysis

The PDM perform well in structural stiffness due to its closed-loop structure. Meanwhile, the closed-loop structure brings more over-constraints, which is necessary for the mobility and force analysis. Next, the over-constrained analysis of the 4-DOF PDM will be derived in detail. The joint type and number are shown in Table I.

The number of over-constraints on the 4-DOF PDM is calculated as follows:

$$t = 3S + 4U + 5R + 5P + A - 6n = 9 \tag{1}$$

https://doi.org/10.1017/S0263574723000929 Published online by Cambridge University Press

3. Kinematic analysis

Kinematic analysis is an indispensable step in the evaluation and application. Therefore, position, velocity, and acceleration analysis of the 4-DOF PDM are presented in this section. In the following, the kinematics of the hybrid manipulator is solved in modules. As shown in Fig. 1, the module-1 represents the operating mechanism, and the module-2 denotes the driving mechanisms, including the 1st, 2nd RPR limbs and the 3rd, 4th SPU limbs. Meanwhile, the module-1 is solved prior to the module-2.

3.1. Inverse position analysis

3.1.1. Inverse position of module-1

Inverse position analysis determines the positions of each limb when the position and orientation of the MP are given. Any vector in the frame $\boldsymbol{P}$-xyz can map to the frame $\boldsymbol{A}$-xyz.

$$\boldsymbol{R} = \boldsymbol{T}\boldsymbol{R}' + \boldsymbol{P} \tag{2}$$

in which

$$\boldsymbol{T} = \boldsymbol{R}(z_0, \alpha)\, \boldsymbol{R}(x_0, \gamma) \tag{3}$$

$$\boldsymbol{P} = \begin{bmatrix} p_x & p_y & p_z \end{bmatrix}^T \tag{4}$$

where $\boldsymbol{T}$ and $\boldsymbol{P}$ denote the orientation matrix and the position vector of the MP, respectively.

For the 1st and 2nd driving limbs, the position vector $R_{3i}(i = 1, 2)$ with respect to the frame $\boldsymbol{A}$-xyz can be obtained based on the homogeneous transformation. In addition, the position vector R_{2i} with respect to the frame $\boldsymbol{A}$-xyz can be expressed by θ_{1i}. We can derive the closed-loop motion equation as

$$\boldsymbol{R}_{1i}\boldsymbol{R}_{2i} = \boldsymbol{R}_{1i}\boldsymbol{R}_{3i} + \boldsymbol{R}_{3i}\boldsymbol{R}_{2i} \tag{5}$$

Eq. (5) can be simplified as follows

$$a_{1i} \cos\theta_{1i} + b_{1i} \sin\theta_{1i} = d_{1i} \tag{6}$$

in which

$$\theta_{1i} = a\tan 2(b_{1i}, a_{1i}) \pm a\tan 2\left(\sqrt{a_{1i}^2 + b_{1i}^2 - d_{1i}^2}, d_{1i}\right) \tag{7}$$

where atan2 stands for four-quadrant inverse tangent function. a_{1i}, b_{1i}, and d_{1i} represent the simplified values of Eq. (5), and their expressions are detailed in Appendix B.

3.1.2. Inverse position of module-2

According to the constraint relationship, the length of l_{1i} can be obtained

$$l_{1i} = \|\boldsymbol{R}_{2i}\boldsymbol{R}_{4i}\| \tag{8}$$

Similar to Eq. (8), the position vector of $U_{2j}(j = 3, 4)$ with respect to the frame $\boldsymbol{O}$-xyz can be obtained. We can derive the length of l_{2j} as

$$l_{2j} = \left\|\boldsymbol{U}_{2j}\boldsymbol{S}_{2j}\right\| \tag{9}$$

3.2. Velocity and acceleration analysis

The displacement of the prismatic joint is given by Eqs. (8) and (9). However, to derive the inverse dynamic formulation for the 4-DOF PDM with Newton–Euler method, the positions, velocities, and accelerations of all bodies in the hybrid manipulator are required to be derived. In the following, we will derive the inverse kinematics in detail.

https://doi.org/10.1017/S0263574723000929 Published online by Cambridge University Press

3.2.1. Velocity and acceleration of module-1

The angular velocity, acceleration, and linear acceleration of the MP can be obtained

$$\boldsymbol{a}_{mp} = \boldsymbol{a}_{mp}^{\tau} + \boldsymbol{a}_{mp}^{n} \tag{10}$$

in which

$$\begin{aligned} \boldsymbol{a}_{mp}^{\tau} &= \boldsymbol{\varepsilon}_{mp} \times \boldsymbol{r}_{R_4,P} \\ \boldsymbol{a}_{mp}^{n} &= \boldsymbol{\omega}_{mp} \times \left(\boldsymbol{\omega}_{mp} \times \boldsymbol{r}_{R_4,P}\right) \end{aligned} \tag{11}$$

where $\boldsymbol{\omega}_{mp}$ and $\boldsymbol{\varepsilon}_{mp}$ represent the angular velocity and acceleration of the MP, respectively. $\boldsymbol{a}_{mp}^{n}$ and $\boldsymbol{a}_{mp}^{\tau}$ denote the normal and tangential acceleration of the MP, respectively.

For the operating mechanism, θ_{2i} can be written as follows:

$$\theta_{2i} = a\cos\left(P_{R_{3i}} - P_{R_{2i}}\right) / r_{3i} \tag{12}$$

Furthermore, differentiating Eq. (12) with respect to time yields

$$\begin{aligned} \dot{\theta}_{2i} &= \left(v_{R_{2i}} - v_{R_{3i}}\right) / \left(r_{3i} s\theta_{2i}\right) \\ \ddot{\theta}_{2i} &= \left(a_{R_{2i}} - a_{R_{3i}} - r_{3i} c\theta_{2i} \dot{\theta}_{2i}^{2}\right) / \left(r_{3i} s\theta_{2i}\right) \end{aligned} \tag{13}$$

Since the operating mechanism is a planar mechanism, the angular velocity and acceleration of l_{3i} can be written as follows:

$$\begin{aligned} \boldsymbol{\omega}_{r3i} &= \begin{bmatrix} 0 & 0 & \dot{\theta}_{2i} \end{bmatrix}^{T} \\ \boldsymbol{\varepsilon}_{r3i} &= \begin{bmatrix} 0 & 0 & \ddot{\theta}_{2i} \end{bmatrix}^{T} \end{aligned} \tag{14}$$

Similarly, the acceleration of the operating mechanism can be written as

$$\boldsymbol{a}_{r3i} = \boldsymbol{a}_{r3i}^{\tau} + \boldsymbol{a}_{r3i}^{n} + \boldsymbol{a}_{R_{2i}} \tag{15}$$

in which

$$\begin{aligned} \boldsymbol{a}_{r3i}^{\tau} &= \boldsymbol{\omega}_{r3i} \times \boldsymbol{r}_{3i} \\ \boldsymbol{a}_{r3i}^{n} &= \boldsymbol{\omega}_{r3i} \times \left(\boldsymbol{\omega}_{r3i} \times \boldsymbol{r}_{3i}\right) \\ \boldsymbol{a}_{R_{2i}} &= \boldsymbol{a}_{R_{2i}}^{\tau} + \boldsymbol{a}_{R_{2i}}^{n} \end{aligned} \tag{16}$$

3.2.2. Velocity and acceleration of module-2

The Euler angle of the 1st and 2nd driving limbs can be written as follows:

$$\alpha_{li} = a\tan 2(b_{li}, a_{li}) \tag{17}$$

The angular velocity and angular acceleration of l_i can be obtained by differentiating Eq. (17). Similar to Eq. (14), the angular velocity and acceleration vector can be expressed as

$$\begin{aligned} \boldsymbol{\omega}_{li} &= \begin{bmatrix} 0 & 0 & \omega_{li} \end{bmatrix}^{T} \\ \ddot{\boldsymbol{\alpha}}_{li} &= \begin{bmatrix} 0 & 0 & \ddot{\alpha}_{li} \end{bmatrix}^{T} \end{aligned} \tag{18}$$

Furthermore, the acceleration at the center of mass of the cylinder can be written as follows:

$$\boldsymbol{a}_{li1} = \boldsymbol{a}_{li1}^{t} + \boldsymbol{a}_{li1}^{n} \tag{19}$$

in which

$$\begin{aligned} \boldsymbol{a}_{li1}^{t} &= \boldsymbol{\alpha}_{li} \times \boldsymbol{r}_{i1} \\ \boldsymbol{a}_{li1}^{n} &= \boldsymbol{\omega}_{li} \times \left(\boldsymbol{\omega}_{li} \times \boldsymbol{r}_{i1}\right) \end{aligned} \tag{20}$$

Similarly, the acceleration at the center of mass of the piston can be written as

$$\boldsymbol{a}_{li2} = \boldsymbol{a}_{li2}^{\tau} + \boldsymbol{a}_{li2}^{n} + \boldsymbol{a}_{li2}^{k} \tag{21}$$

https://doi.org/10.1017/S0263574723000929 Published online by Cambridge University Press

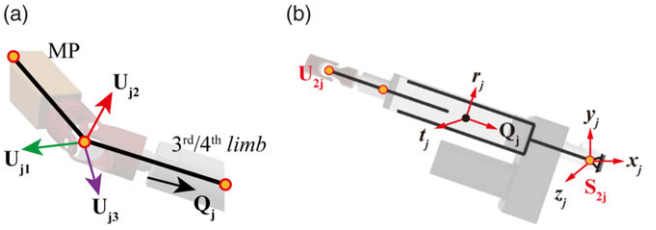

Figure 4. *Coordinate frame of the U joint.*

in which

$$\begin{aligned} \boldsymbol{a}_{li2}^{\tau} &= \boldsymbol{\alpha}_{li} \times \boldsymbol{r}_{i2} \\ \boldsymbol{a}_{li2}^{n} &= \boldsymbol{\omega}_{li} \times (\boldsymbol{\omega}_{li} \times \boldsymbol{r}_{i2}) \\ \boldsymbol{a}_{li2}^{k} &= 2\boldsymbol{\omega}_{li} \times \boldsymbol{v}_{r} \end{aligned} \tag{22}$$

where $\boldsymbol{a}_{li2}^{k}$ denote the Coriolis acceleration of the piston in 1st and 2nd driving limbs.

For the U joint in the 3rd and 4th driving limbs, many papers assume that the angular velocity and acceleration are perpendicular to the direction along SPU limb for the convenience of derivation. In this paper, the actual angular velocity and acceleration values are obtained through geometric constraint relationship. The local coordinate frame attached to the U joint is shown in Fig. 4.

The coordinate systems of the 3rd and 4th driving limbs are shown in Fig. 4. First, we assume that the orientation matrix of the 3rd and 4th driving limbs frame $\boldsymbol{Q}$-xyz with respect to the reference frame $\boldsymbol{A}$-xyz can be derived in terms of three rotational angles α, β, and γ satisfying the z-x-z convention:

$$\begin{aligned} &\boldsymbol{R}_z(\alpha)\,\boldsymbol{R}_x(\beta)\,\boldsymbol{R}_z(\gamma) \\ &= \begin{bmatrix} \mathrm{c}\alpha\mathrm{c}\gamma - \mathrm{s}\alpha\mathrm{c}\beta\mathrm{s}\gamma & -\mathrm{c}\alpha\mathrm{s}\gamma - \mathrm{s}\alpha\mathrm{c}\beta\mathrm{c}\gamma & \mathrm{s}\alpha\mathrm{s}\beta \\ \mathrm{s}\alpha\mathrm{c}\gamma + \mathrm{c}\alpha\mathrm{c}\beta\mathrm{s}\gamma & -\mathrm{s}\alpha\mathrm{s}\gamma + \mathrm{c}\alpha\mathrm{c}\beta\mathrm{c}\gamma & -\mathrm{c}\alpha\mathrm{s}\beta \\ \mathrm{s}\beta\mathrm{s}\gamma & \mathrm{s}\beta\mathrm{c}\gamma & \mathrm{c}\beta \end{bmatrix} \end{aligned} \tag{23}$$

where s and c represent the abbreviations of sine and cosine, respectively. In addition, $\boldsymbol{Q}_j$ can be obtained by the following equation:

$$\boldsymbol{Q}_j = \frac{\boldsymbol{U}_{2j}\boldsymbol{S}_{2j}}{\left\|\boldsymbol{U}_{2j}\boldsymbol{S}_{2j}\right\|} \tag{24}$$

Hence, taking Eqs. (23) and (24) into account, the Euler angle of l_{2j} can be written as follows:

$$\begin{aligned} \alpha &= -a\tan 2\left(\boldsymbol{Q}_j(1,1), \boldsymbol{Q}_j(2,1)\right) \\ \beta &= a\cos\left(\boldsymbol{Q}_j(3,1)\right) \end{aligned} \tag{25}$$

Differentiating Eq. (25) with respect to time, $\dot{\alpha}, \ddot{\alpha}, \dot{\beta}$, and $\ddot{\beta}$ can be obtained, respectively. To derive the Euler angle γ, it is necessary to supplement equations based on the geometric constraint relationship. Hence, we can derive $\boldsymbol{U}_{j2}$ as

$$\begin{aligned} \boldsymbol{U}_{j2} &= \boldsymbol{Q}_j \times \boldsymbol{U}_{j1} \\ \boldsymbol{U}_{j2}^{e} &= \frac{\boldsymbol{U}_{j2}}{|\boldsymbol{U}_{j2}|} \end{aligned} \tag{26}$$

where vector $\boldsymbol{U}_{j1}$ denotes the axis along with the MP at the U joint, vector $\boldsymbol{U}_{j2}$ denotes the axis along with the 3rd and 4th SPU limb. From Eqs. (23) to (26), γ can be expressed as

$$\gamma = a\cos\left(\boldsymbol{U}_{j2}^{e}(3,1)\right) / \sin(\beta) \tag{27}$$

Differentiating Eq. (27) with respect to time, $\dot{\gamma}, \ddot{\gamma}$ can be obtained, respectively. In addition, $\boldsymbol{U}_{j3}$ can be obtained by vector cross product, which is the direction of the constrained torque at the U joint.

$$\boldsymbol{U}_{j3} = \boldsymbol{U}_{j1} \times \boldsymbol{U}_{j2} \tag{28}$$

https://doi.org/10.1017/S0263574723000929 Published online by Cambridge University Press

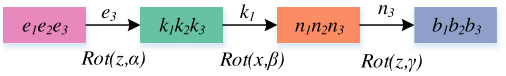

Figure 5. *Mapping of Euler angles rate to angular velocity.*

Furthermore, to obtain the angular velocity of each link, we need to map the Euler angles rate to the angular velocity. The mapping principle is shown in Fig. 5.

According to the above transformation, Eq. (29) can be obtained

$$\begin{bmatrix} \omega_x \\ \omega_y \\ \omega_z \end{bmatrix} = rot(z,\alpha)\ rot(x,\beta) \begin{bmatrix} 0 \\ 0 \\ \dot{\gamma} \end{bmatrix} + rot(z,\alpha) \begin{bmatrix} \dot{\beta} \\ 0 \\ 0 \end{bmatrix} + \begin{bmatrix} 0 \\ 0 \\ \dot{\alpha} \end{bmatrix} \tag{29}$$

By sorting out Eq. (29), the following equation can be obtained

$$\boldsymbol{\omega}_{lj} = \boldsymbol{J}_t \begin{bmatrix} \dot{\alpha}_{lj} & \dot{\beta}_{lj} & \dot{\gamma}_{lj} \end{bmatrix}^T \tag{30}$$

in which

$$\boldsymbol{J}_t = \begin{bmatrix} 0 & c\alpha_{lj} & s\alpha_{lj}s\beta_{lj} \\ 0 & s\alpha_{lj} & -c\alpha_{lj}s\beta_{lj} \\ 1 & 0 & c\beta_{lj} \end{bmatrix} \tag{31}$$

Furthermore, differentiating Eq. (30) with respect to time, the following equation can be obtained

$$\boldsymbol{\varepsilon}_{lj} = \boldsymbol{J}_t \begin{bmatrix} \ddot{\alpha}_{lj} & \ddot{\beta}_{lj} & \ddot{\gamma}_{lj} \end{bmatrix}^T + \dot{\boldsymbol{J}}_t \begin{bmatrix} \dot{\alpha}_{lj} & \dot{\beta}_{lj} & \dot{\gamma}_{lj} \end{bmatrix}^T \tag{32}$$

For the 1st and 2nd driving limbs, $\boldsymbol{L}_{1i}$ represents the vector between the two joints R_{2i} and R_{4i}

$$\boldsymbol{L}_{1i} = \boldsymbol{r}_{2i} - \boldsymbol{r}_{4i} \tag{33}$$

where $\boldsymbol{r}_{2i}$ and $\boldsymbol{r}_{4i}$ represent the vectors of joint R_{2i} and R_{4i} with respect to frame $\{\boldsymbol{A}\}$, respectively. Moreover, use $\boldsymbol{Q}_{1i}$ to denote the unit vector along $\boldsymbol{L}_{1i}$

$$\boldsymbol{Q}_i = \boldsymbol{L}_{1i}/l_{1i} \tag{34}$$

The velocity of any point in the moving frame can be obtained by vector cross-product

$$\boldsymbol{V} = \boldsymbol{V}' + \boldsymbol{\omega} \times \boldsymbol{r} \tag{35}$$

where $\boldsymbol{\omega}$ and $\boldsymbol{V}$ represent the angular velocity and the linear velocity of the MP, respectively.

Differentiating Eq. (7) with respect to time yields:

$$\dot{\theta}_{1i} = \boldsymbol{J}_{0i}\dot{\boldsymbol{P}} \tag{36}$$

where $\dot{\boldsymbol{P}}$ denotes the velocity matrix of the MP.

Similarly, linear velocity of l_i by differentiating Eq. (8) can be obtained

$$\dot{l}_{1i} = \boldsymbol{J}_{1i}\dot{\boldsymbol{P}} \tag{37}$$

The linear acceleration of the MP can be obtained by the following formula

$$\boldsymbol{A} = \boldsymbol{A}' + \boldsymbol{\varepsilon} \times \boldsymbol{r} + \boldsymbol{\omega} \times (\boldsymbol{\omega} \times \boldsymbol{r}) \tag{38}$$

where $\boldsymbol{\varepsilon}$ denotes the angular acceleration of the MP.

Furthermore, differentiating Eq. (36) with respect to time yields:

$$\ddot{\theta}_{1i} = \boldsymbol{J}_{0i}\ddot{\boldsymbol{P}} + \dot{\boldsymbol{P}}^T\boldsymbol{H}_{0i}\dot{\boldsymbol{P}} \tag{39}$$

where $\ddot{\boldsymbol{P}}$ denotes the acceleration matrix of the MP.

Similarly, linear acceleration of l_i can be obtained as time derivative of Eq. (37)

$$\ddot{l}_{1i} = \boldsymbol{J}_{1i}\ddot{\boldsymbol{P}} + \dot{\boldsymbol{P}}^T\boldsymbol{H}_{1i}\dot{\boldsymbol{P}} \tag{40}$$

https://doi.org/10.1017/S0263574723000929 Published online by Cambridge University Press

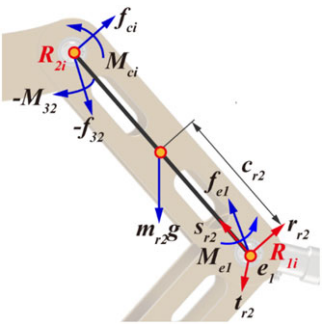

Figure 6. *Forces and moments analysis for the link-2.*

For the 3rd and 4th driving limbs, the linear velocity can be calculated by Eq. (35)

$$\boldsymbol{V}_{U2j} = \boldsymbol{G}_p^{U_{2j}} \dot{\boldsymbol{P}} \tag{41}$$

$$l_{2j}^2 = \boldsymbol{L}_{2j} \cdot \boldsymbol{L}_{2j} \tag{42}$$

Differentiating Eq. (42) with respect to time, the following formula can be obtained

$$l_{2j}\dot{l}_{2j} = \boldsymbol{L}_{2j} \cdot \boldsymbol{V}_{2j} \tag{43}$$

Hence, the velocity of the l_{2j} can be expressed as follows:

$$\dot{l}_{2j} = \boldsymbol{Q}_j^T \boldsymbol{V}_{U_{2j}} = \boldsymbol{J}_{1j} \dot{\boldsymbol{P}} \tag{44}$$

in which

$$\boldsymbol{J}_{1j} = \boldsymbol{Q}_j^T \boldsymbol{G}_p^{U_{2j}} \tag{45}$$

According to the Eq. (38), the following formula can be obtained

$$\boldsymbol{A}_{U_{2j}} = \boldsymbol{G}_p^{U_{2j}} \ddot{\boldsymbol{P}} + \dot{\boldsymbol{P}}^T \boldsymbol{H}_{0j} \dot{\boldsymbol{P}} \tag{46}$$

Furthermore, linear acceleration of l_{2j} can be obtained by differentiating Eq. (44)

$$\ddot{l}_{2j} = \boldsymbol{Q}_j^T \boldsymbol{A}_{U_{2j}} + \left(\boldsymbol{V}_{U_{2j}}^T \boldsymbol{V}_{U_{2j}} - \dot{l}_{2j}^2 \right) / l_{2j} \tag{47}$$

Hence, the acceleration of the l_{2j} can be written as follows:

$$\ddot{l}_{2j} = \boldsymbol{J}_{2j} \ddot{\boldsymbol{P}} + \dot{\boldsymbol{P}}^T \boldsymbol{H}_{1j} \dot{\boldsymbol{P}} \tag{48}$$

So far, all the kinematic parameters required for the inverse dynamics are determined. In the next section, attention will be paid on the deduction of dynamic equations of the 4-DOF PDM.

4. Dynamic analysis

For the structural design, the driving forces and the constrained forces/moments should be calculated simultaneously to evaluate the force condition of the system. Therefore, this section presents the dynamics modeling of the 4-DOF PDM. First, the force analysis of individual bodies, limbs are derived with Newton–Euler method. Then, based on the flexibility matrix and compatible deformation are employed to supplementary equations. Similar to the kinematic analysis, the dynamic derivation of the 4-DOF PDM is also solved in modules.

4.1. Forces and moments analysis for the module-1

The forces and moments analysis diagrams of link r_{21} are given in Fig. 6. The reaction forces and moments at fixed points R_{1i} are denoted by $\boldsymbol{f}_{e1}$ and $\boldsymbol{M}_{e1}$. The forces and moments at moving points R_{2i} are denoted by $\boldsymbol{f}_{32}$ and $\boldsymbol{M}_{32}$, respectively.

https://doi.org/10.1017/S0263574723000929 Published online by Cambridge University Press

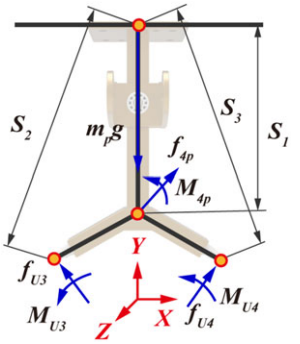

Figure 7. *Forces and moments analysis for the moving platform.*

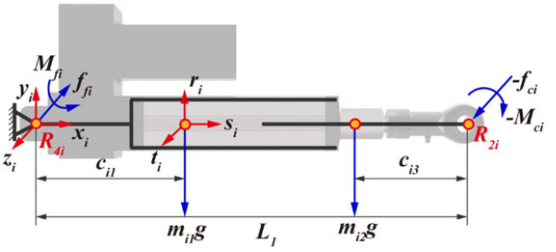

Figure 8. *Forces and moments analysis for 1st and 2nd driving limbs.*

The Newton–Euler equations for link r_{21} are given as

$$\begin{aligned}\sum \boldsymbol{F}_{ext} &= \boldsymbol{f}_{ci} - \boldsymbol{f}_{32} + \boldsymbol{f}_{e1} + m_{r2}\boldsymbol{g} = m_{r2}\boldsymbol{a}_{r2}\\ \sum {}^{ci1}\boldsymbol{n}_{ext} &= {}^{A}\boldsymbol{I}_{cr2}\dot{\boldsymbol{\omega}}_{r2} + \boldsymbol{\omega}_{r2} \times {}^{A}\boldsymbol{I}_{cr2}\boldsymbol{\omega}_{r2}\\ &\quad + c_{r2}\left(-\boldsymbol{s}_{r2} \times \boldsymbol{f}_{e1}\right) + c_{r2}\left(\boldsymbol{s}_{r2} \times \boldsymbol{f}_{ci}\right) + c_{r2}\left(\boldsymbol{s}_{r2} \times -\boldsymbol{f}_{32}\right) + \boldsymbol{M}_{ci} - \boldsymbol{M}_{32} + \boldsymbol{M}_{e1}\end{aligned} \tag{49}$$

Similar to link r_{21}, other links' forces and moments of the operating mechanism can be obtained. Furthermore, the forces and moments analysis for the MP are shown in Fig. 7.
The Newton–Euler equations for MP are given as

$$\begin{aligned}\sum \boldsymbol{F}_{ext} &= \boldsymbol{f}_{4p} + \boldsymbol{f}_{U3} + \boldsymbol{f}_{U4} + m_p\boldsymbol{g} = m_p\boldsymbol{a}_p\\ \sum \boldsymbol{n}_{ext} &= \boldsymbol{S}_1 \times \boldsymbol{f}_{4p} + \boldsymbol{S}_2 \times \boldsymbol{f}_{U3} + \boldsymbol{S}_3 \times \boldsymbol{f}_{U4} + \boldsymbol{M}_{U3} + \boldsymbol{M}_{U4} + \boldsymbol{M}_{4p}\\ &= {}^{A}\boldsymbol{I}_p\dot{\boldsymbol{\omega}}_p + \boldsymbol{\omega}_p \times {}^{A}\boldsymbol{I}_p\boldsymbol{\omega}_p\end{aligned} \tag{50}$$

4.2. Forces and moments analysis of the module-2

Assume that each driving limb consists of two parts, the cylinder and the piston, where the velocities and accelerations of their centers of masses are determined in Section 3. Assume that the centers of masses of the cylinder and the piston are located at a distance of c_{i1} and c_{i3}, and their masses are denoted by m_{i1} and m_{i2}, respectively. Moreover, consider that the cylinder and the pistons are symmetric about their axes, and their centers of masses lie at their midlengths.

The forces and moments analysis diagrams of 1st and 2nd driving limb are given in Fig. 8. The reaction forces and moments at fixed points R_{4i} are denoted by $\boldsymbol{f}_{fi}$ and $\boldsymbol{M}_{fi}$. The forces and moments at moving points R_{2i} are denoted by $\boldsymbol{f}_{ci}$ and $\boldsymbol{M}_{ci}$, and the internal forces and moments between cylinders and pistons are denoted by $\boldsymbol{f}_{mi}$ and $\boldsymbol{M}_{mi}$, respectively.

https://doi.org/10.1017/S0263574723000929 Published online by Cambridge University Press

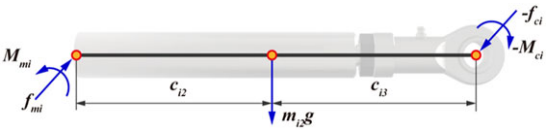

Figure 9. *Forces and moments analysis for the piston.*

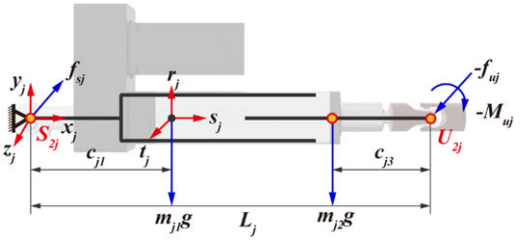

Figure 10. *Forces and moments analysis for 3rd and 4th driving limbs.*

The Newton–Euler equation for 1st and 2nd driving limbs are given as

$$\left({}^{A}\boldsymbol{I}_{ci_1}+{}^{A}\boldsymbol{I}_{ci_2}\right)\dot{\boldsymbol{\omega}}_i+\boldsymbol{\omega}_i\times\left({}^{A}\boldsymbol{I}_{ci_1}+{}^{A}\boldsymbol{I}_{ci_2}\right)\boldsymbol{\omega}_i=\boldsymbol{M}_{fi}+m_{i2}(L_1-c_{i3})\,(\boldsymbol{s}_i\times(\boldsymbol{g}-\boldsymbol{a}_{i2}))+m_{i1}c_{i1}(\boldsymbol{s}_i\times(\boldsymbol{g}-\boldsymbol{a}_{i1}))+L_1\left(\boldsymbol{s}_i\times-\boldsymbol{f}_{ci}\right)-\boldsymbol{M}_{ci}\tag{51}$$

where ${}^{A}\boldsymbol{I}_{ci_1}$ denotes the inertia matrix of the cylinder evaluated at a frame parallel to $\{\boldsymbol{A}\}$ located at point c_{i1}. Since the cylinder is moving with respect to this frame, this matrix can be evaluated by rotation rule from the inertia matrix easily obtained about $\{\boldsymbol{A}_i\}$ attached to the cylinder at point c_{i1}. This can be done through the following transformation:

$${}^{A}\boldsymbol{I}_{ci_1}={}^{A}\boldsymbol{R}_{Ai}\,{}^{A}\boldsymbol{I}_{ci_1}\,{}^{A}\boldsymbol{R}_{Ai}^{T}\tag{52}$$

Note the formula of vector mixed product is as follows:

$$(\boldsymbol{a}\times\boldsymbol{b})\cdot\boldsymbol{c}=(\boldsymbol{b}\times\boldsymbol{c})\cdot\boldsymbol{a}=(\boldsymbol{c}\times\boldsymbol{a})\cdot\boldsymbol{b}\tag{53}$$

Multiply $\boldsymbol{t}_i$ on both sides of Eq. (51), and the following equation can be obtained

$$\boldsymbol{f}_{\boldsymbol{ci}}^{ri}=m_{i1}c_{i1}\boldsymbol{r}_i\cdot(\boldsymbol{g}-\boldsymbol{a}_{i1})+m_{i2}(L_1-c_{i3})\,\boldsymbol{r}_i\cdot(\boldsymbol{g}-\boldsymbol{a}_{i2})-\boldsymbol{t}_i\cdot\left(\left({}^{A}\boldsymbol{I}_{ci1}+{}^{A}\boldsymbol{I}_{ci2}\right)\dot{\boldsymbol{\omega}}_i\right)-\boldsymbol{t}_i\cdot\left(\boldsymbol{\omega}_i\times\left({}^{A}\boldsymbol{I}_{ci1}+{}^{A}\boldsymbol{I}_{ci2}\right)\boldsymbol{\omega}_i\right)\tag{54}$$

Forces and moments analysis for piston are shown in Fig. 9.

The Newton–Euler equations for piston are given as

$$\sum\boldsymbol{F}_{ext}=m_{i2}\boldsymbol{a}_{i2}=\boldsymbol{f}_{mi}-\boldsymbol{f}_{ci}+m_{i2}\boldsymbol{g}\tag{55}$$

By multiplying $\boldsymbol{s}_i$ on both sides of Eq. (55), formulas that only include driving force and kinematic parameters can be derived as follows:

$$f_{ci}^{s}=\tau_i+m_{i2}\boldsymbol{g}\cdot\boldsymbol{s}_i-m_{i2}\boldsymbol{a}_{i2}\cdot\boldsymbol{s}_i\tag{56}$$

The forces and moments analysis diagrams of 3rd and 4th driving limbs are given in Fig. 10. The reaction forces and moments at fixed points S_{2j} are denoted by $\boldsymbol{f}_{sj}$ and $\boldsymbol{M}_{sj}$. The forces and moments at moving points U_{2j} are denoted by $\boldsymbol{f}_{uj}$ and $\boldsymbol{M}_{uj}$, and the internal forces and moments between cylinders and pistons are denoted by $\boldsymbol{f}_{mj}$ and $\boldsymbol{M}_{mj}$, respectively.

The Newton–Euler equation for 3rd and 4th driving limbs are given as

$$\left({}^{A}\boldsymbol{I}_{cj1}+{}^{A}\boldsymbol{I}_{cj2}\right)\dot{\boldsymbol{\omega}}_j+\boldsymbol{\omega}_j\times\left({}^{A}\boldsymbol{I}_{cj1}+{}^{A}\boldsymbol{I}_{cj2}\right)\boldsymbol{\omega}_j=-L_j\left(\boldsymbol{s}_j\times\boldsymbol{f}_{uj}\right)-m_{i2}\left(L_j-c_{i3}\right)\boldsymbol{s}_j\times(\boldsymbol{a}_{i2}-\boldsymbol{g})-m_{i1}L_{31}\boldsymbol{s}\times(\boldsymbol{a}_{i1}-\boldsymbol{g})-M_{uj}\boldsymbol{t}_{uj}\tag{57}$$

https://doi.org/10.1017/S0263574723000929 Published online by Cambridge University Press

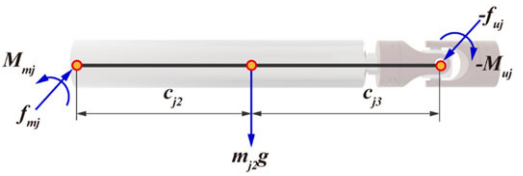

Figure 11. *Forces and moments analysis for the piston.*

According to Eq. (56), the following equation can be obtained

$$M_{uj} = \frac{\boldsymbol{s}_j \cdot \left(\left({}^{A}\boldsymbol{I}_{ci1} + {}^{A}\boldsymbol{I}_{ci2}\right)\dot{\boldsymbol{\omega}}_j\right) + \boldsymbol{s}_j \cdot \left(\boldsymbol{\omega}_j \times \left({}^{A}\boldsymbol{I}_{ci1} + {}^{A}\boldsymbol{I}_{ci2}\right)\boldsymbol{\omega}_j\right)}{-\boldsymbol{s}_j \cdot \boldsymbol{t}_{uj}} \tag{58}$$

Vector cross-product formula is as follows:

$$\boldsymbol{a} \times (\boldsymbol{b} \times \boldsymbol{c}) = (\boldsymbol{c} \cdot \boldsymbol{a})\,\boldsymbol{b} - (\boldsymbol{a} \cdot \boldsymbol{b})\,\boldsymbol{c} \tag{59}$$

Furthermore, by multiplying $\boldsymbol{s}$ on both sides of Eq. (57) and combing Eq. (59), the following equation can be obtained

$$\boldsymbol{f}_{uj} = \left(\boldsymbol{s}_j \cdot \boldsymbol{f}_{uj}\right) + \frac{1}{L_j}\boldsymbol{s}_j \times \begin{pmatrix} \left(m_{j2}\left(L_j - c_{j3}\right)\boldsymbol{s}_j \times \left(\boldsymbol{a}_{j2} - \boldsymbol{g}\right)\right) + \left(c_{j1}m_{j1}\boldsymbol{s}_j \times \left(\boldsymbol{a}_{j1} - \boldsymbol{g}\right)\right) \\ + \left(\left({}^{A}\boldsymbol{I}_{cj1} + {}^{A}\boldsymbol{I}_{cj2}\right)\dot{\boldsymbol{\omega}}_j\right) + \left(\boldsymbol{\omega}_j \times \left({}^{A}\boldsymbol{I}_{cj1} + {}^{A}\boldsymbol{I}_{cj2}\right)\boldsymbol{\omega}_j\right) + M_{uj}\boldsymbol{t}_{uj} \end{pmatrix} \tag{60}$$

The forces and moments analysis of piston are shown in Fig. 11.
The Newton–Euler equations for piston segments are given as

$$\boldsymbol{f}_{mj} - \boldsymbol{f}_{uj} + m_{j2}\boldsymbol{g} = m_{j2}\boldsymbol{a}_{j2} \tag{61}$$

Multiplying $\boldsymbol{s}$ on both sides of Eq. (61) and substituting Eq. (60) into Eq. (61), we have

$$\begin{aligned} \boldsymbol{f}_{uj} = {} & \left(\tau_j + \boldsymbol{s}_j \cdot m_{j2}\boldsymbol{g} - \boldsymbol{s}_j \cdot m_{j2}\boldsymbol{a}_{j2}\right)\boldsymbol{s}_j \\ & + \frac{1}{L_j}\boldsymbol{s}_j \times \begin{pmatrix} \left(L_j - c_{j2}\right)\boldsymbol{s}_j \times m_{j2}\left(\boldsymbol{g} - \boldsymbol{a}_{j2}\right) + c_{j1}\boldsymbol{s}_j \times m_{j1}\left(\boldsymbol{g} - \boldsymbol{a}_{j1}\right) \\ + \left({}^{A}\boldsymbol{I}_{cj1} + {}^{A}\boldsymbol{I}_{cj2}\right)\dot{\boldsymbol{\omega}}_j + \boldsymbol{\omega}_j \times \left({}^{A}\boldsymbol{I}_{cj1} + {}^{A}\boldsymbol{I}_{cj2}\right)\boldsymbol{\omega}_j + M_{uj}\boldsymbol{t}_{uj} \end{pmatrix} \end{aligned} \tag{62}$$

To sum up, there are 84 equations based on the Newton–Euler method, but 93 unknown variables need to be solved due to the over-constraints of the 4-DOF PDM. In the next section, nine compatibility equations are introduced considering the flexibility matrix and compatible deformation.

5. Deformation compatibility analysis

Based on the redundant constraint analysis in Section 2.2, we know that the 4-DOF PDM possesses nine passive redundant constraints, although the four actuator driving forces can be obtained with the classical method, the internal force analysis of this manipulator is still a statically indeterminate problem, and therefore the joint reaction forces cannot be uniquely determined. In this section, to obtain the unique solution, the over-constrained direction is analyzed by the screw theory, and the flexibility of the limbs is considered and the deformation compatibility condition is introduced.

5.1. Link's elastic deformation

In this paper, the link is regarded as a homogeneous rod. As shown in Fig. 12, when the end link is subjected to external forces $\boldsymbol{F} = [F_x\ F_y\ F_z\ M_x\ M_y\ M_z]^T$, corresponding six-dimensional deformation will be formed, including tension, torsion, and bending.

The relation between the external force $\boldsymbol{F}$ and the corresponding small deflection $\boldsymbol{X}$ along the applied force axis can be written as follows

https://doi.org/10.1017/S0263574723000929 Published online by Cambridge University Press

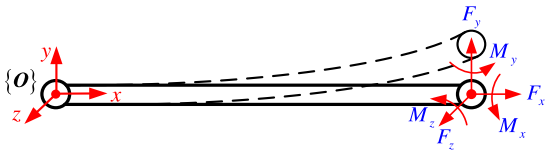

Figure 12. *Schematic diagram of deformation at the end of uniform bar with regular section.*

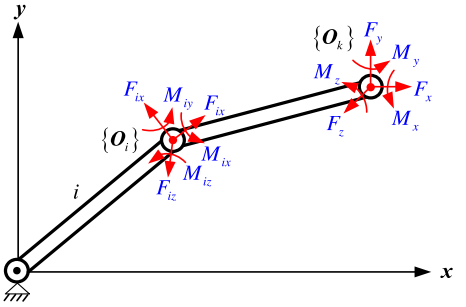

Figure 13. *Deformation diagram of two link ends with regular section.*

$$\boldsymbol{X} = \boldsymbol{C}\boldsymbol{F} \tag{63}$$

in which

$$\boldsymbol{C} = \begin{bmatrix} \frac{l}{EA} & 0 & 0 & 0 & 0 & 0 \\ 0 & \frac{l^3}{3EI_z} & 0 & 0 & 0 & \frac{l^2}{2EI_z} \\ 0 & 0 & \frac{l^3}{3EI_y} & 0 & -\frac{l^2}{2EI_y} & 0 \\ 0 & 0 & 0 & \frac{l}{GI_p} & 0 & 0 \\ 0 & 0 & -\frac{l^2}{2EI_y} & 0 & \frac{l}{EI_y} & 0 \\ 0 & \frac{l^2}{2EI_z} & 0 & 0 & 0 & \frac{l}{EI_z} \end{bmatrix} \tag{64}$$

where $\boldsymbol{C}$ represents the flexibility matrix with respect to frame $\{\boldsymbol{O}\}$. I_y, I_z, and I_p denote cross-section inertia parameters of the rod, respectively. l and A are rod length and cross-sectional area of rod. E and G represent elastic modulus and shear modulus of materials, respectively.

For the two-link mechanism depicted in Fig. 13, according to the force balance condition of the rod, the Jacobian matrix $\boldsymbol{J}$ as the projection of forces $\boldsymbol{F}_i$ to external forces $\boldsymbol{F}$ are given

$$\boldsymbol{F}_i = \boldsymbol{J}_i\boldsymbol{F} \tag{65}$$

in which

$$\boldsymbol{J}_k = \begin{pmatrix} {}^{oi}_{ok}\boldsymbol{R} & \boldsymbol{0}_{3\times3} \\ \boldsymbol{S}\left({}^{oi}\boldsymbol{P}_{ok}\right){}^{oi}_{ok}\boldsymbol{R} & {}^{oi}_{ok}\boldsymbol{R} \end{pmatrix} \tag{66}$$

where ${}^{oi}_{ok}\boldsymbol{R}$ represents rotational transformation matrix between frame $\{\boldsymbol{O}_k\}$ and frame $\{\boldsymbol{O}_i\}$. ${}^{oi}\boldsymbol{P}_{ok}$ is the position vector with respect to the frame $\{\boldsymbol{O}_k\}$. $\boldsymbol{S}({}^{oi}\boldsymbol{P}_{ok})$ denotes antisymmetric matrix of position vector ${}^{oi}\boldsymbol{P}_{ok}$.

https://doi.org/10.1017/S0263574723000929 Published online by Cambridge University Press

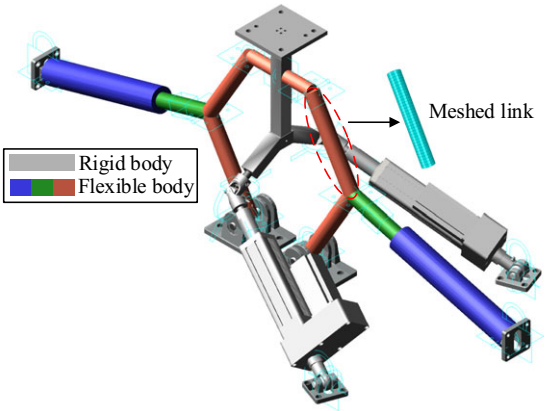

Figure 14. *Rigid–flexible coupling model of the 4-DOF PDM.*

Referring to Eq. (63), the relation between the force $\boldsymbol{F}_i$ and the corresponding small deflection $\boldsymbol{X}_i$ along the applied force axis can be written as follows

$$\boldsymbol{X}_i = \boldsymbol{C}_i \boldsymbol{F}_i \tag{67}$$

Hence, the deformation of end link $\Delta \boldsymbol{X}_i$ caused by the deformation of the rod i is as follows

$$\Delta \boldsymbol{X}_i = \boldsymbol{J}_i^T \boldsymbol{C}_i \boldsymbol{F}_i \tag{68}$$

Therefore, the deformation of the end link under the external force $\boldsymbol{F}$ can be derived by the sum of linear deformation of all rod i

$$\boldsymbol{X} = \sum \Delta \boldsymbol{X}_i = \sum \boldsymbol{J}_i^T \boldsymbol{C}_i \boldsymbol{J}_i \boldsymbol{F} \tag{69}$$

5.2. Rigid-flexible coupling simulation

As indicated above, the 4-DOF PDM possesses nine passive redundant constraints. Since the SPU limb own six degrees-of-freedom, the over-constraints are caused by other links besides the SPU limbs. In this section, based on the screw theory, the over-constrained direction is analyzed. Moreover, the over-constraints were verified via the co-simulation with ABAQUS and ADAMS software. First, the flexible links are meshed by hexahedron elements in ABAQUS, and the mnf files of the meshed links are obtained via ABAQUS. Then, loading the link files, rigid links are replaced with flexible bodies in ADAMS. The simulation model is shown as Fig. 14.

From the above analysis, we know that over-constraints are caused by operating mechanism and two RPR limbs. In order to supplement the deformation coordination equations, we need to further determine the direction of over-constraints. Based on the screw theory, the constraint screw of the limb is as follows:

$$\begin{aligned} \$_1^{rr} &= \begin{bmatrix} 0 & 0 & 1 & 0 & 0 & 0 \end{bmatrix} \\ \$_2^{rr} &= \begin{bmatrix} 0 & 0 & 0 & 1 & 0 & 0 \end{bmatrix} \\ \$_3^{rr} &= \begin{bmatrix} 0 & 0 & 0 & 0 & 1 & 0 \end{bmatrix} \end{aligned} \tag{70}$$

As shown in Fig. 15, the operating mechanism and two RPR limbs possess the constrained force along $\boldsymbol{z}$-axis and constrained couples around $\boldsymbol{x}$-axis, $\boldsymbol{y}$-axis, which means each link in the operating mechanism and two RPR limb own three over-constrained motions.

https://doi.org/10.1017/S0263574723000929 Published online by Cambridge University Press

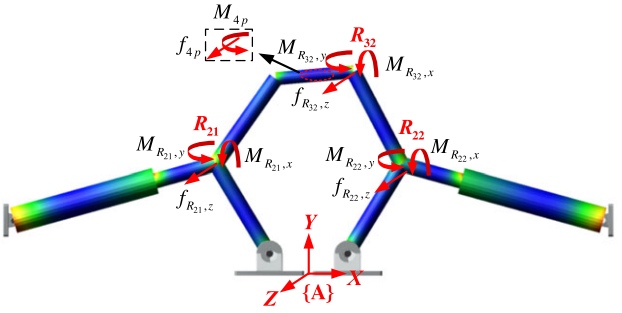

Figure 15. *Schematic diagram of over-constrained direction analysis.*

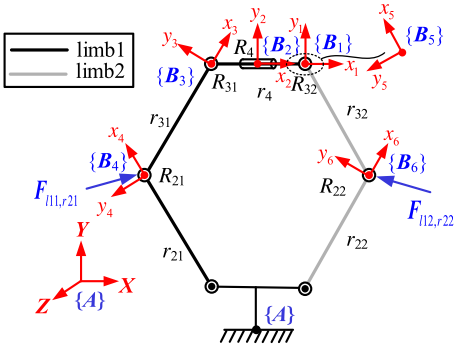

Figure 16. *Limbs 1 and 2 deformation analysis.*

5.3. Deformation compatibility equation

In this section, on the condition of the numbers and direction of over-constraints, we derive the deformation compatibility equation in detail. First, the operating mechanism and two RPR limbs are divided into three modules. Then derive the deformation of each module according to the link's elastic deformation in Section 5.1. Finally, the deformation compatibility equations are derived at joints R_{21}, R_{22}, and R_{32}.

The elastic deformation of limbs 1 and 2 at joint R_{32} as shown in Fig. 16.

Referring to Eq. (65), we have

$$^{B2}\boldsymbol{F}_{R4} = \boldsymbol{J}_{B2,B1}{}^{B1}\boldsymbol{F}_{r32,r4} + \boldsymbol{J}_{B2,A}{}^{A}\boldsymbol{F}_{4p} \tag{71}$$

$$^{B3}\boldsymbol{F}_{r4,r31} = \boldsymbol{J}_{B3,B2}{}^{B2}\boldsymbol{F}_{R4} \tag{72}$$

$$^{B4}\boldsymbol{F}_{r31,r21} = \boldsymbol{J}_{B4,B3}{}^{B3}\boldsymbol{F}_{r4,r31} \tag{73}$$

where $^{B1}\boldsymbol{F}_{r32,r4}$ is the force applied to link r_4 by link r_{32} with respect to the frame $\{\boldsymbol{A}\}$. $\boldsymbol{J}_{B2,A}$ represents the transformation matrix between frame $\{\boldsymbol{B}_2\}$ and frame $\{\boldsymbol{A}\}$.

Based on the Eq. (69), the elastic deformations of the links r_{21} and r_{31} at the joint R_{31} with respect to the frame $\{\boldsymbol{B}_3\}$ are

$$^{B3}\boldsymbol{\delta}_{R31} = \boldsymbol{C}_1{}^{B3}\boldsymbol{F}_{r4,r31} + \boldsymbol{J}^{T}_{B4,B3}\left(\boldsymbol{C}_1{}^{B4}\boldsymbol{F}_{r31,r21} + \boldsymbol{C}_1{}^{B4}\boldsymbol{F}_{l11,r21}\right) \tag{74}$$

Hence, the elastic deformation of the links r_{21}, r_{31}, and r_4 at the joint R_{32} with respect to the frame $\{\boldsymbol{A}\}$ are

$$^{A}\boldsymbol{\delta}_{R32\_\mathrm{lim}\,b1} = \boldsymbol{J}^{T}_{B1,A}\left(\boldsymbol{J}^{T}_{B3,B1}{}^{B3}\boldsymbol{\delta}_{R31} + \boldsymbol{J}^{T}_{B2,B1}\boldsymbol{C}_2{}^{B2}\boldsymbol{F}_{R4} + \boldsymbol{C}_2{}^{B1}\boldsymbol{F}_{r32,r4}\right) \tag{75}$$

Similarly, the elastic deformation of limb2 at R_{32} is given as

$$^{B6}\boldsymbol{F}_{r32,r22} = \boldsymbol{J}_{B6,B5}{}^{B5}\boldsymbol{F}_{r32,r4} \tag{76}$$

https://doi.org/10.1017/S0263574723000929 Published online by Cambridge University Press

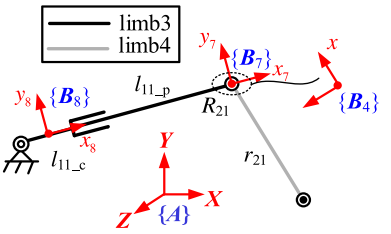

Figure 17. *Limbs 3 and 4 deformation analysis.*

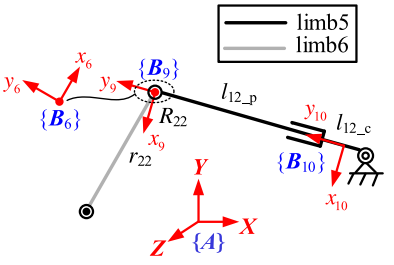

Figure 18. *Limbs 5 and 6 deformation analysis.*

$$^{R22}\boldsymbol{\delta}_{R22} = \boldsymbol{C}_1{}^{B6}\boldsymbol{F}_{r32,r22} + \boldsymbol{C}_1{}^{B6}\boldsymbol{F}_{l12,r22} \tag{77}$$

$$^{A}\boldsymbol{\delta}_{R32\_limb2} = \boldsymbol{J}_{B5,A}\left(\boldsymbol{J}_{B6,B5}{}^{R22}\boldsymbol{\delta}_{R22} + \boldsymbol{C}_1{}^{B5}\boldsymbol{F}_{r4,r32}\right) \tag{78}$$

The deformation caused by limbs 3 and 4 at joint R_{32} as shown in Fig. 17.
Referring to Eq. (69), the elastic deformation of limb 3 at joint R_{21} is given as

$$^{A}\boldsymbol{\delta}_{R21\_limb3} = \boldsymbol{J}_{B7,A}^{T}\left(\boldsymbol{J}_{B8,B7}^{T}\boldsymbol{C}_4\boldsymbol{J}_{B8,B7}\left(-{}^{B7}\boldsymbol{F}_{l11,r21}\right) + \boldsymbol{C}_3\left(-{}^{B7}\boldsymbol{F}_{l11,r21}\right)\right) \tag{79}$$

Similarly, the elastic deformation of limb 4 at joint R_{21} is given as

$$^{A}\boldsymbol{\delta}_{R21\_limb4} = \boldsymbol{J}_{B4,A}^{T}\left(\boldsymbol{C}_1{}^{B4}\boldsymbol{F}_{l2,l1} + \boldsymbol{C}_1{}^{B4}\boldsymbol{F}_{l7,l1}\right) \tag{80}$$

The deformation caused by limbs 5 and 6 at joint R_{32} as shown in Fig. 18.
Based on the Eq. (69), the elastic deformation of limb 5 at joint R_{22} are given as

$$^{A}\boldsymbol{\delta}_{R22\_limb5} = \boldsymbol{J}_{B9,A}^{T}\left(\boldsymbol{J}_{B10,B9}^{T}\boldsymbol{C}_6\boldsymbol{J}_{B10,B9}\left(-{}^{B9}\boldsymbol{F}_{l12,r22}\right) + \boldsymbol{C}_5\left(-{}^{B7}\boldsymbol{F}_{l12,r22}\right)\right) \tag{81}$$

Similarly, the elastic deformation of limb 6 at joint R_{22} are given as

$$^{A}\boldsymbol{\delta}_{R22\_limb6} = \boldsymbol{J}_{B6,A}^{T}\left(\boldsymbol{C}_1{}^{B6}\boldsymbol{F}_{r32,r22} + \boldsymbol{C}_1{}^{B6}\boldsymbol{F}_{l12,r22}\right) \tag{82}$$

The deformations of the operating mechanism and two RPR limbs have to be compatible with each other to satisfy the geometric constraints. Hence, translational deformation along z and rotational deformation about x and y axis at joints R_{21}, R_{22}, R_{32} should be equal, namely

$$\begin{aligned} &^{A}\boldsymbol{\delta}_{R32\_limb1}(k,1) = {}^{A}\boldsymbol{\delta}_{R32\_limb2}(k,1) \\ &^{A}\boldsymbol{\delta}_{R21\_limb3}(k,1) = {}^{A}\boldsymbol{\delta}_{R21\_limb4}(k,1)\ (k=3,4,5) \\ &^{A}\boldsymbol{\delta}_{R22\_limb5}(k,1) = {}^{A}\boldsymbol{\delta}_{R22\_limb6}(k,1) \end{aligned} \tag{83}$$

So far, the complete dynamics models with constrained forces/moments of the over-constrained 4-DOF PDM with sub-closed chains are established. The actuation forces and constrained forces/moments can be obtained simultaneously, which is essential for structure design. Also, clearance and friction can be easily integrated into the system equation.

https://doi.org/10.1017/S0263574723000929 Published online by Cambridge University Press

6. Simulation and experiment

We set the trajectory of the end-effector of the manipulator with respect to the inertial reference frame ***P***-*xyz* as follows:

$$\begin{aligned} x(t) &= S_x\left(\frac{t}{T} - \frac{1}{2\pi}\sin\left(2\pi\frac{t}{T}\right)\right) \; t \in [0, T] \\ y(t) &= S_y\left(\frac{t}{T} - \frac{1}{2\pi}\sin\left(2\pi\frac{t}{T}\right)\right) \; t \in [0, T] \\ \alpha(t) &= S_\alpha\left(\frac{t}{T} - \frac{1}{2\pi}\sin\left(2\pi\frac{t}{T}\right)\right) \; t \in [0, T] \\ \gamma(t) &= S_\gamma\left(\frac{t}{T} - \frac{1}{2\pi}\sin\left(2\pi\frac{t}{T}\right)\right) \; t \in [0, T] \end{aligned} \tag{84}$$

where S_x and S_y denote the displacement along the x-axis and y-axis with respect to the fixed reference coordinate system, S_α and S_γ denote the angle along the x-axis and z-axis with respect to the fixed reference coordinate system, respectively.

6.1. Simulation validation

According to the derivation of the above formula, the displacements, velocities, accelerations, driving forces, and all constraint forces/moments of the 4-DOF PDM are obtained. The numerical simulation results are qualitatively consistent with the theoretical results. As shown in Fig. 19, $l_{1,a}$, $v_{1,a}$, and $a_{1,a}$ ($i = 1, 2, 3, 4$) denote the theoretical displacements, velocities, and accelerations of the slider respectively. $l_{i,n}$, $v_{i,n}$, and $a_{i,n}$ ($i = 1, 2, 3, 4$) denote the numerical displacements, velocities, and accelerations of the slider, respectively.

The results of co-simulation with ADAMS and ABAQUS are shown in Fig. 14. Figure 20 shows the active forces computed by the proposed method and ADAMS; Figure 21 shows the active forces computed by the proposed method and Lagrangian method; Figure 22(a) and (b) show the constraint forces/moments in the over-constrained direction at joints R_{32} and R_{21}, respectively. $f^a_{i\_z}$, $m^a_{i\_x}$ and $m^a_{i\_y}(i = 1, 2)$ represent the theoretical value and $f^n_{i\_z}$, $m^n_{i\_x}$ and $m^n_{i\_y}(i = 1, 2)$ represent the simulation value.

It is assumed that the cylinders and pistons are symmetrically distributed in this paper. That is, the influence of the eccentricity of the electric cylinder on the constraint torque at the U-joint is not considered. In order to verify the influence of acceleration on the constraint torque and driving force at the U-joint, the constraint torques at the U-joint are calculated when the maximum translational acceleration along y-axis is up to 50, 500, and 1000 mm/s^2. Moreover, the driving forces are solved with and without constraint torque at the U-joint, and the driving forces error percentage are plotted as shown in Fig. 23(b).

6.2. Experiment validation

According to the CAD model displayed in Fig. 1, a physical prototype has been built for the motion control experiment. As shown in Fig. 24, actuators are driven by the electric piston-cylinder, which are connected to an embedded controller (CX5130) made by the company Beckhoff through an Ethercat bus. Based on the position loop mode PID controller to achieve the target trajectory, it is one of the commonly used controllers in academic research and industrial products. The motion control experiment based on PID controller is shown in Figure 25. The measured values of displacements, velocities, and accelerations of the four driving limbs are shown in Fig. 26, which are consistent with the theoretical calculation.

In this paper, the control cycle of the embedded controller (CX5130) is 2 ms. As shown in Fig. 26, the measured position and velocity of the four driving limbs are consistent with the theoretical value, but the lag of phase is 20 ms. Due to the short control cycle, the position signal obtained by the encoder

https://doi.org/10.1017/S0263574723000929 Published online by Cambridge University Press

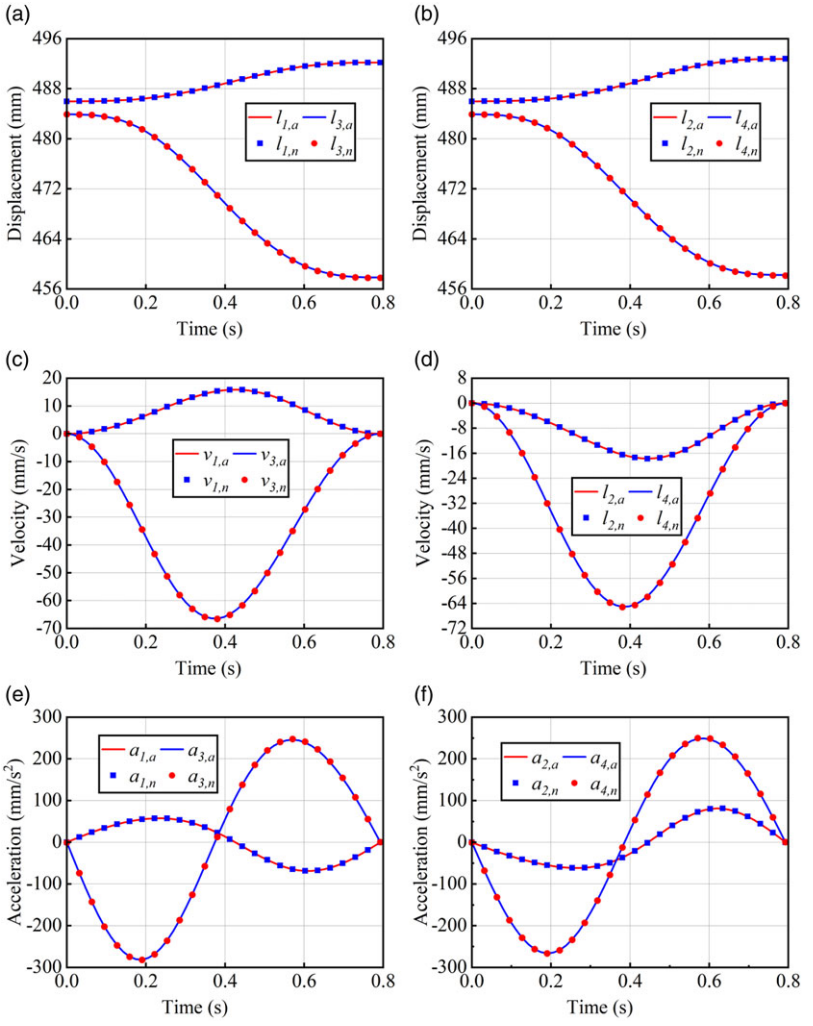

Figure 19. *Numerical and theoretical results of displacement/velocity/acceleration.*

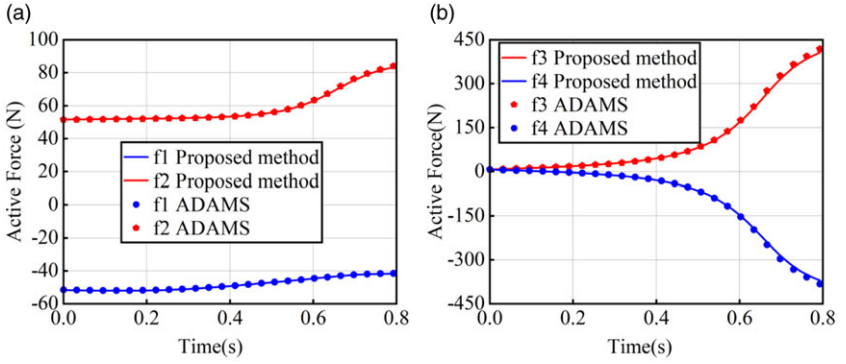

Figure 20. *Active forces computed by the proposed method and ADAMS.*

https://doi.org/10.1017/S0263574723000929 Published online by Cambridge University Press

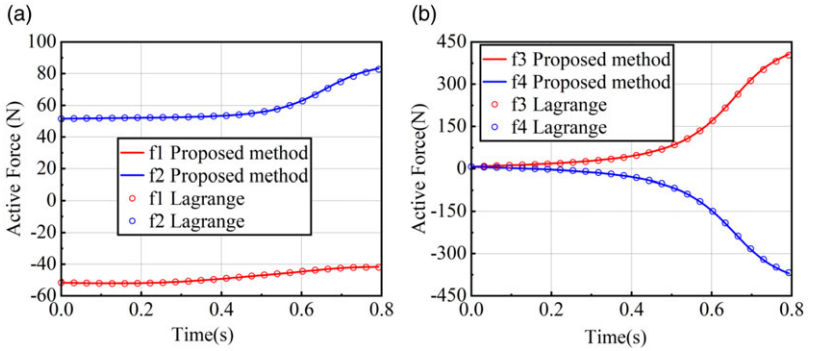

Figure 21. *Active forces computed by the proposed method and Lagrangian method.*

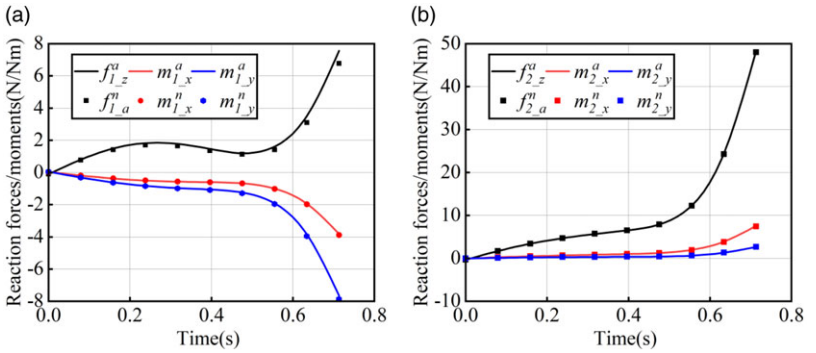

Figure 22. *Partial constraint forces/moments simulation and theoretical value.*

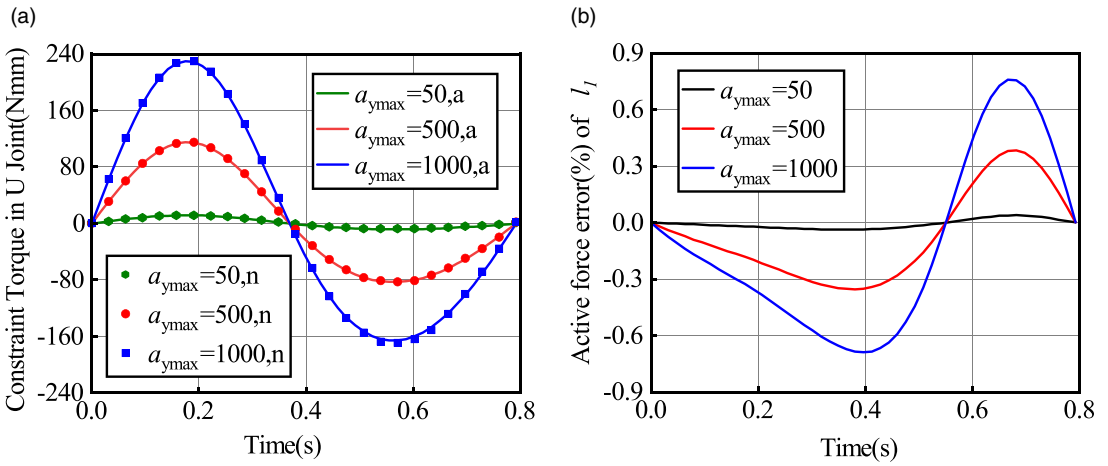

Figure 23. *Constraint torque at U-joint and driving force error percentage under different accelerations.*

https://doi.org/10.1017/S0263574723000929 Published online by Cambridge University Press

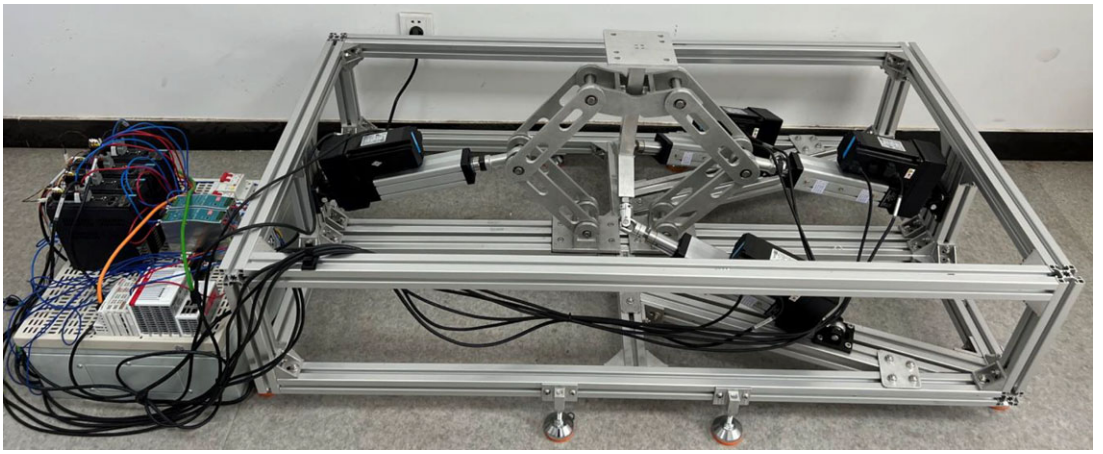

Figure 24. *Physical prototype and control system.*

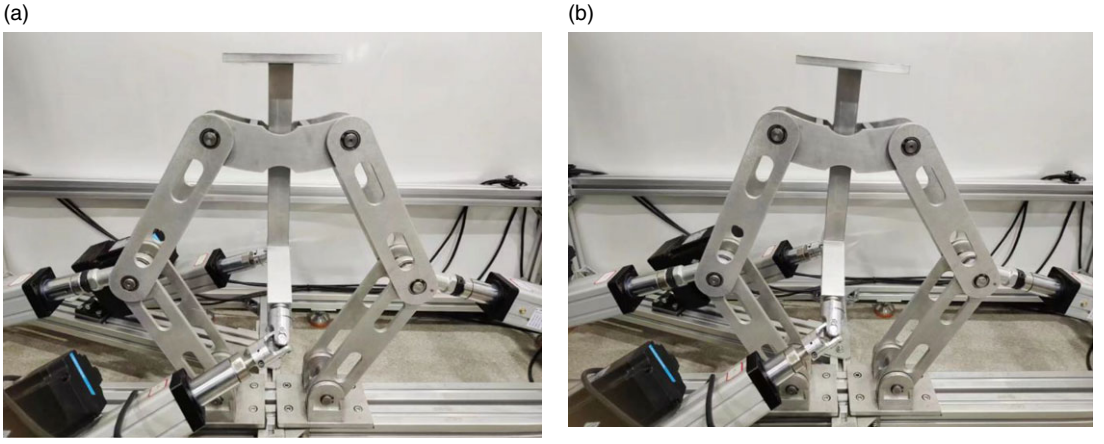

Figure 25. *Trajectory planning based on classical PID control.*

undergoes two differential and filtering processes, resulting in significant signal distortion. As shown in Fig. 26, the measured acceleration not only have phase lag but also have attenuation in amplitude.

7. Conclusion

In this paper, a 4-DOF over-constrained PDM with sub-closed chains is proposed and its prototype is developed. By considering the flexibility of the operating mechanism and two RPR limbs, the deformation compatibility condition is introduced to solve a statically indeterminate problem. The actuation forces and constrained forces/moments are obtained simultaneously, which is conducive to the design of the PDM.

In the symmetrical structure of the electric piston-cylinder, the value of constraint moments at the U-joint under different accelerations is analyzed by taking into account its impact on driving forces. According to the results of comparative experiment conducted on the end-effector under different accelerations in a certain direction, the impact on the active force is about 1%, regardless of the constraint moment at the U-joint. The effectiveness of the kinematic model is demonstrated by ADAMS and the experiment based on classical PID control, while that of the dynamic model is confirmed by the co-simulation with MATLAB, ADAMS and ABAQUS. In addition, the actuation forces are also verified by using the Lagrangian method. The present study provides a valuable reference for future study on structural optimization. In future studies, the rigid–flexible coupling dynamic model will

https://doi.org/10.1017/S0263574723000929 Published online by Cambridge University Press

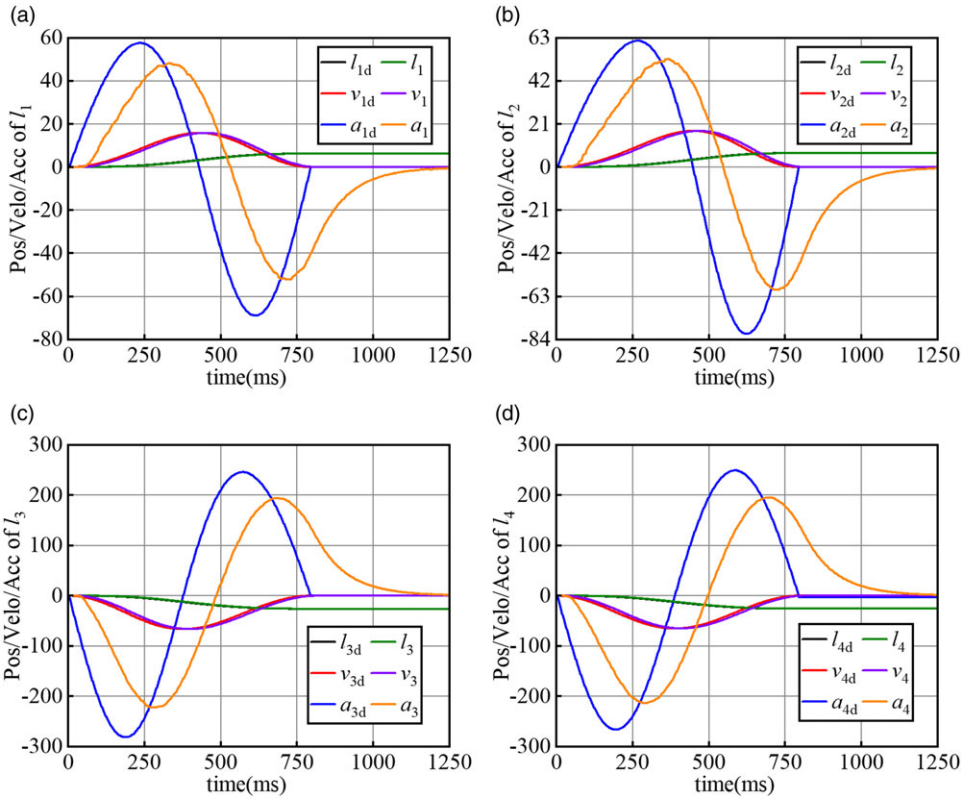

Figure 26. *Measured and theoretical results of displacement/velocity/acceleration.*

also be established to obtain rigid–flexible coupling dynamic characteristics and an accurate constraint forces/moments.

Availability of data and materials. The datasets used and/or analyzed during the current study are available from the corresponding author on reasonable request.

Author contribution. Yangyang Huang, Jinzhu Zhang, and Xiaoyan Xiong conceived and designed the study. Shengxiang Liu conducted data gathering. Yangyang Huang wrote the article.

Financial support. The authors would like to acknowledge (1) Project (51905367) supported by The National Nature Science Foundation of China, (2) Project (201901D211011) supported by The Foundation of Applied Basic Research General Youth Program of Shanxi.

Competing interests. The authors declare no competing interests exist.

Ethical approval. Not applicable.

References

[1] W. Yang, H. Ding and A. Kecskeméthy, "Structural synthesis towards intelligent design of plane mechanisms: Current status and future research trend," *Mech. Mach. Theory* **171**, 104715 (2022).

[2] H. Q. Shi, J. Z. Zhang, T. Wang, R. Li and Q. X. Huang, "Mechanism design and kinematic analysis of a bioinspired 5-DOF parallel driving mechanism," *Mech. Mach. Theory* **181**, 105178 (2023).

[3] J. Li, F. Ye, N. Y. Shen, Z. R. Wang and L. Geng, "Dimensional synthesis of a 5-DOF hybrid robot," *Mech. Mach. Theory* **150**, 103865 (2020).

[4] B. Hu, Y. G. Shi, L. Z. Xu and P. Bai, "Reconsideration of terminal constraint/mobility and kinematics of 5-DOF hybrid manipulators formed by one 2R1T PM and one RR SM," *Mech. Mach. Theory* **149**, 103837 (2020).

[5] S. Gupta, S. Gupta and S. Ekta, "A novel modular approach for kinematic modeling and analysis of planar hybrid manipulators," *J. Mech. Des.* **143**(9), 1–46 (2021).

https://doi.org/10.1017/S0263574723000929 Published online by Cambridge University Press

[6] L. R. Zhou, J. F. Li, F. Y. Li, Q. Meng, J. Li and X. S. Xu, "Energy consumption model and energy efficiency of machine tools: A comprehensive literature review," *J. Clean. Prod.* **112**, 3721–3734 (2015).
[7] T. Tang and J. Zhang, "Conceptual design and kinetostatic analysis of a modular parallel kinematic machine-based hybrid machine tool for large aeronautic components," *Robot. Comput.-Integr. Manuf.* **57**, 1–16 (2019).
[8] M. Y. Wei, S. A. Fang and J. W. Liu, "Design and implementation of a new training flight simulator system," *Sensors* **22**(20), 7933 (2022).
[9] Z. Q. Lu, D. Wu, H. Ding and L. Q. Chen, "Vibration isolation and energy harvesting integrated in a Stewart platform with high static and low dynamic stiffness," *Appl. Math. Model.* **89**, 249–267 (2020).
[10] M. To and P. Webb, "An improved kinematic model for calibration of serial robots having closed-chain mechanisms," *Robotica* **30**(6), 963–971 (2012).
[11] H. N. Nguyen, J. Zhou, H. J. Kang and T. D. Le, "Position accuracy improvement of robots having closed-chain mechanisms," *Lect. Notes Comput. Sci.* **8589**, 285–292 (2014).
[12] M. Chen, Q. Zhang, X. R. Qin and Y. T. Sun, "Kinematic, dynamic, and performance analysis of a new 3-DOF over-constrained parallel mechanism without parasitic motion," *Mech. Mach. Theory* **162**, 104365 (2021).
[13] Y. Xu, W. Liu, J. Yao and Y. Zhao, "A method for force analysis of the overconstrained lower mobility parallel mechanism," *Mech. Mach. Theory* **88**, 31–48 (2015).
[14] Y. J. Zhao, F. Gao, W. M. Li, W. Liu and X. C. Zhao, "Development of 6-DOF parallel seismic simulator with novel redundant actuation," *Mechatronics* **19**(3), 422–427 (2009).
[15] J. Wu, T. M. Li, J. S. Wang and L. P. Wang, "Stiffness and natural frequency of a 3-DOF parallel manipulator with consideration of additional leg candidates," *Robot. Auton. Syst.* **61**(8), 868–875 (2013).
[16] X. L. Shan, Y. H. Li, H. T. Liu and T. Huang, "Residual vibration reduction of high-speed pick-and-place parallel robot using input shaping," *Chin. J. Mech. Eng.* **16**(1), 35 (2022).
[17] X. Li-xin and L. Yong-gang, "Investigation of joint clearance effects on the dynamic performance of a planar 2-DOF pick-and-place parallel manipulator," *Robot. Comput.-Integr. Manuf.* **30**(1), 62–73 (2014).
[18] Z. Chen, L. Xu, W. Zhang and Q. Li, "Closed-form dynamic modeling and performance analysis of an over-constrained 2PUR-PSR parallel manipulator with parasitic motions," *Nonlinear Dyn.* **96**(1), 517–534 (2019).
[19] X. L. Chen, L. K. Wu, Y. Deng and Q. Wang, "Dynamic response analysis and chaos identification of 4-UPS-UPU flexible spatial parallel mechanism," *Nonlinear Dyn.* **87**(4), 2311–2324 (2016).
[20] P. Flores, J. Ambrósio, J. C. P. Claro and H. M. Lankarani, *Kinematics and Dynamics of Multibody Systems with Imperfect Joints: Models and Case Studies*, vol. 34 (Springer, Berlin, Heidelberg, 2008).
[21] Q. Tian, P. Flores and H. M. Lankarani, "A comprehensive survey of the analytical, numerical and experimental methodologies for dynamics of multibody mechanical systems with clearance or imperfect joints," *Mech. Mach. Theory* **122**, 1–57 (2018).
[22] P. Flores, J. Ambrósio, J. C. P. Claro, H. M. Lankarani and C. S. Koshy, "Lubricated revolute joints in rigid multibody systems," *Nonlinear Dyn.* **56**(3), 277–295 (2009).
[23] M. McGrath, D. Howard and R. Baker, "A Lagrange-based generalised formulation for the equations of motion of simple walking models," *J. Biomech.* **55**, 139–143 (2017).
[24] F. Marques, I. Roupa, M. T. Silva, P. Flores and H. M. Lankarani, "Examination and comparison of different methods to model closed loop kinematic chains using Lagrangian formulation with cut joint, clearance joint constraint and elastic joint approaches," *Mech. Mach. Theory* **160**, 104294 (2021).
[25] B. Dasgupta and T. S. Mruthyunjaya, "Closed-form dynamic equations of the general Stewart platform through the Newton-Euler approach," *Mech. Mach. Theory* **33**(7), 993–1012 (1998).
[26] M. Chen, Q. Zhang, X. R. Qin and Y. T. Sun, "Kinematic, dynamic, and performance analysis of a new 3-DOF over-constrained parallel mechanism without parasitic motion," *Mech. Mach. Theory* **162**(5), 104365 (2021).
[27] Y. J. Zhao and F. Gao, "Inverse dynamics of the 6-DOF out-parallel manipulator by means of the principle of virtual work," *Robotica* **27**(2), 259–268 (2008).
[28] S. Pedrammehr, S. Nahavandi and H. Abdi, "Closed-form dynamics of a hexarot parallel manipulator by means of the principle of virtual work," *Acta Mech. Sinica* **34**(5), 883–895 (2018).
[29] Y. Xu, W. Liu, J. Yao and Y. Zhao, "A method for force analysis of the overconstrained lower mobility parallel mechanism," *Mech. Mach. Theory* **88**, 31–48 (2015).
[30] Z. M. Bi and B. Kang, "An inverse dynamic model of over-constrained parallel kinematic machine based on Newton-Euler formulation," *ASME J. Dyn. Sys., Meas. Control* **136**(4), 041001 (2014).
[31] G. Chen, W. Yu, Q. Li and H. Wang, "Dynamic modeling and performance analysis of the 3-PRRU 1T2R parallel manipulator without parasitic motion," *Nonlinear Dyn.* **90**(1), 339–353 (2017).
[32] H. Elgolli, A. Houidi, A. Mlika and L. Romdhane, "Analytical analysis of the dynamic of a spherical parallel manipulator," *Int. J. Adv. Manuf. Technol.* **101**(1–4), 859–871 (2019).
[33] J. Yi, T. M. Li and L. P. Wang, "Research on the dynamic model of an over-constrained parallel mechanism," *J. Mech. Eng.* **49**(17), 123–129 (2013).
[34] M. X. Wang, H. T. Liu and T. Huang, "An approach for the lightweight design of a 3-SPR parallel mechanism," *J. Mech. Robot.* **9**(5), 051016 (2017).
[35] M. Sharifzadeh, A. Arian, A. Salimi, M. T. Masouleh and A. Kalhor, "An experimental study on the direct & indirect dynamic identification of an over-constrained 3-DOF decoupled parallel mechanism," *Mech. Mach. Theory* **116**, 178–202 (2017).
[36] X. Chen, S. Jiang and T. Wang, "Dynamic modeling and analysis of multi-link mechanism considering lubrication clearance and flexible components," *Nonlinear Dyn.* **107**(4), 3365–3383 (2022).

[37] M. Shi, B. Rong, J. Liang, W. Zhao and H. Pan, "Dynamics analysis and vibration suppression of a spatial rigid-flexible link manipulator based on transfer matrix method of multibody system," *Nonlinear Dyn.* **111**(2), 1139–1159 (2023).
[38] L. Xiao, F. Yan, T. Chen, S. Zhang and S. Jiang, "Study on nonlinear dynamics of rigid-flexible coupling multi-link mechanism considering various kinds of clearances," *Nonlinear Dyn.* **111**(4), 3279–3306 (2023).
[39] M. To and P. Webb, "An improved kinematic model for calibration of serial robots having closed-chain mechanisms," *Robotica* **30**(6), 963–971 (2012).
[40] H. N. Nguyen, J. Zhou, H. J. Kang and T. D. Le, "Position accuracy improvement of robots having closed-chain mechanisms," *Lect. Notes Comput. Sci.* **8589**, 285–292 (2014).
[41] Y. M. Li and S. Staicu, "Inverse dynamics of a 3-PRC parallel kinematic machine," *Nonlinear Dyn.* **67**(2), 1031–1041 (2011).
[42] P. J. Shao, Z. Wang, S. Yang and Z. Liu, "Dynamic modeling of a two-DOF rotational parallel robot with changeable rotational axes," *Mech. Mach. Theory* **131**, 318–335 (2019).

Appendix A

The kinematic and dynamic parameters of the PDM virtual prototype used in the simulation are as follows (default in mm unit):

$$r_0 = 73.5, r_1 = 180, r_{2i} = r_{3i} = 240, r_4 = 180, g_1 = 110.10719, g_2 = 346.80127, g_3 = 285.26279,$$
$$g_4 = 99.91525, E = 7.1705e + 4\ (Mpa)\ , u = 0.33, G = E/\ (2\ (1 + \mu))\ , D_1 = 35, D_2 = 60, D_3 = 30$$

Appendix B

$$\begin{aligned} a_{1i} &= r_{2i}\left(x_{R3i} + (-1)^{i+1} r_1/2\right) \\ b_{1i} &= r_{2i}(y_{R3i} - n_1) \\ d_{li} &= r_{2i}^2/2 - \left(x_{R3i} + (-1)^{i+1} r_1/2\right)^2/2 + (y_{R3i} - n_1)^2/2 \\ &\quad - (r_{3i})^2/2 + \left(x_{R3i} + (-1)^{i+1} r_1/2\right)\left(x_{R3i} + (-1)^{i+1} r_1/2\right) \end{aligned}$$

Table II. *The inertial parameters of the PDM.*

Parameters	Value (kg)	Parameter	Value (kgm^{2}10^{-4})
m_{l11}	6.8385	$\boldsymbol{I}_{cl11}$	diag[309 252 88.4]
m_{l12}	0.6824	$\boldsymbol{I}_{cl12}$	diag[49.3 49.3 0.99]
m_{l21}	6.8385	$\boldsymbol{I}_{cl21}$	diag[309 252 88.4]
m_{l22}	0.6824	$\boldsymbol{I}_{cl22}$	diag[49.3 49.3 0.99]
m_{l31}	6.8385	$\boldsymbol{I}_{cl31}$	diag[106.9 87.2 30.6]
m_{l32}	0.6215	$\boldsymbol{I}_{cl32}$	diag[30.9 30.9 0.94]
m_{l41}	6.8385	$\boldsymbol{I}_{cl41}$	diag[106.9 87.2 30.6]
m_{l42}	0.6215	$\boldsymbol{I}_{cl42}$	diag[30.9 30.9 0.94]
m_{r1}	0.5689	$\boldsymbol{I}_{r1}$	diag[46.7 41.1 9.68]
m_{r2}	0.5689	$\boldsymbol{I}_{r2}$	diag[50.9 41.1 13.8]
m_{r3}	0.6887	$\boldsymbol{I}_{r3}$	diag[31.1 25.8 10]
m_{r4}	0.5689	$\boldsymbol{I}_{r4}$	diag[50.9 41.1 13.8]
m_{r5}	0.5689	$\boldsymbol{I}_{r5}$	diag[46.7 41.1 9.68]
m_{mp}	1.8722	$\boldsymbol{I}_{mp}$	diag[347 310 54.8]

Cite this article: Y. Huang, J. Zhang, X. Xiong and S. Liu (2023). "Kinematic and dynamic analysis of a 4-DOF over-constraint parallel driving mechanism with planar sub-closed chains", Robotica **41**, 3137–3159. https://doi.org/10.1017/S0263574723000929